frontiers | Frontiers in Electronics

TYPE Original Research
PUBLISHED 24 February 2025
DOI 10.3389/felec.2025.1507644

OPEN ACCESS

EDITED BY
Afaque Manzoor,
Washington University in St. Louis, United States

REVIEWED BY
Giovanni Bianchi,
Polytechnic University of Milan, Italy
Qiyuan Fu,
Biorobotics Laboratory (BioRob), Switzerland
Jahan Zeb Gul,
Air University, Pakistan

*CORRESPONDENCE
Nathaniel Mengers,
nnm22@case.edu

RECEIVED 08 October 2024
ACCEPTED 31 January 2025
PUBLISHED 24 February 2025

CITATION
Mengers N, Rouse N and Daltorio KA (2025) Stable heteroclinic channels for controlling a simulated aquatic serpentine robot in narrow crevices.
Front. Electron. 6:1507644.
doi: 10.3389/felec.2025.1507644

Stable heteroclinic channels for controlling a simulated aquatic serpentine robot in narrow crevices

Nathaniel Mengers*, Natasha Rouse and Kathryn A. Daltorio

Biologically Inspired Robotics Laboratory, Mechanical and Aerospace Engineering, Case Western Reserve University, Cleveland, OH, United States

Stable Heteroclinic Channels (SHCs) are dynamical systems composed of connected saddle equilibria. This work demonstrates a control system that combines SHCs with movement primitives to enable swimming in a simulated six segment snake robot. We identify control system parameters for lateral undulation, where all joints oscillate with the same amplitude, and anguilliform swimming, where joint amplitudes increase linearly from the head to the tail. Swimming speed is improved by learning SHC movement primitive parameters. We also propose a method for adapting the gait amplitude and frequency with tactile sensor input to accommodate obstacles. Then, we evaluate the relationship between SHC movement primitive parameters and the resulting trajectories. The swimming speed and efficiency of SHC controllers for each gait are compared against a conventional serpenoid controller, which derives joint trajectories from sinusoids. Controllers are evaluated first in an unobstructed environment, then in straight passages of various widths, and finally in 65 randomly generated uneven channels. We find that the amplitudes of joint oscillations scale proportionally with the SHC controller parameters. Due to gait optimization, as well as adaptive amplitude and frequency in response to tactile input, the learned SHC control system exhibits an average 28.8% greater speed than a serpenoid controller that only adapts amplitude during contact. This research demonstrates that SHCs benefit from intuitive tuning like serpenoid control, while also effectively incorporating sensory information to generate smooth kinematic trajectories.

KEYWORDS

stable heteroclinic channels, snake robot, autonomy, central pattern generator, motor primitive, nonlinear control

1 Introduction

Modeling neuroanatomical structures not only supports biological research, but advances robotics by inspiring frameworks for adaptive, flexible control. Motor primitives (MPs) describe fundamental units of actuation that are assembled to produce complex behavior (Giszter, 2015). MP models in robots offer modular (Paraschos et al., 2013), learnable (Kober and Peters, 2009) control with efficient sensor integration (Bonardi et al., 2012). Meanwhile, central pattern generators (CPGs) are neural circuits that produce rhythms without rhythmic input (Ijspeert, 2008) for locomotion and other functions (Sherrington, 1910; Grillner and Wallén, 2010; Cropper et al., 2004). Hierarchical MP and CPG combinations have been proposed for adaptable rhythms in biological (Guertin,

2013) and mechanical contexts (Moreno and Gomez, 2011). However, relationships between MP parameters and resulting behaviors are nonlinear, complicating modification and analysis (Rouse and Daltorio, 2021). We demonstrate that kinematic MPs incorporating Stable Heteroclinic Channels (SHCs), an emerging CPG model (Daltorio et al., 2013; Brecelj and Petrič, 2023a), enable transparent, learnable, and sensor-adaptable control in a simulated swimming snake robot. In obstacle-free and confined environments, we compare speed and efficiency for SHC controllers with a serpenoid controller, which prescribes joint angles via sinusoids. We further show that incorporating tactile sensing improves speed in confined spaces.

MPs have been used to both model animal behavior (Tresch and Bizzi, 1999; Fod et al., 2002; Tagliabue et al., 2015) and plan robot motion (Ijspeert et al., 2013). MPs arise when modular clusters of neurons and muscle cells reliably produce specific kinematic trajectories or force outputs (Giszter, 2015). Dynamic Movement Primitives (DMPs) are a popular framework for constructing kinematic MPs in robots (Paraschos et al., 2013; Hoffmann et al., 2009; Pastor et al., 2009; Schaal, 2006; Kober and Peters, 2009). They rely on sequentially arranged, weighted Gaussian distributions (kernels), where weights are learned from demonstration to produce arbitrary trajectories (Schaal, 2006; Pastor et al., 2009; Kong et al., 2023). Sensory inputs adapt the planned trajectory, allowing robots to interact with their environment Paraschos et al. (2013). Periodically activating kernels yields rhythmic behavior (Ijspeert et al., 2013). The mapping from learned parameters to the planned trajectory is nonlinear (Rouse and Daltorio, 2021). Thus, the controller behaves as a black box, making it difficult to discern how adjusting the weights may influence robot behavior.

Like MPs, CPGs are an important aspect of biological motor function, and have been modeled for robotic control. Biological CPGs can emerge from a pacemaker neuron that rhythmically self excites (Harris-Warrick, 2010; Marder and Eisen, 1984), or mutually inhibitory, modular neuron clusters (e.g., half-center oscillators) (Ijspeert, 2008; Grillner and Wallén, 2010). The peripheral nervous system can modulate rhythms by inhibiting or exciting CPG neurons (Andersson et al., 1978). In addition to modeling neural connections, biomimetic CPG simulate cellular processes using Hodgkin-Huxley (HH) (Simoni and DeWeerth, 2007) dynamics or approximations such as leaky integrators (Yu et al., 2014). More abstract models use limit cycles, or coupled oscillatory differential equations, to approximate neuron clusters without reproducing cellular dynamics (Wang Z. et al., 2017; Ijspeert et al., 2013). Couplings represent relationships between joints, as well as extensors and flexors for a single joint (Thandiackal et al., 2021). Biomimetic models offer insight into mechanisms for rhythmogenesis, while abstractions address neuron cluster interactions (Ijspeert, 2008). Modularity and sensor integration make both types of CPGs attractive tools for rhythmic control in robots (Hunt et al., 2017; Ijspeert et al., 2007).

Segmental robots based on snakes (Wang J. et al., 2017), salamanders (Ijspeert et al., 2007), and worms (Riddle et al., 2023) are useful for examining CPG controllers due to their modular construction and variety of motor patterns. Biomimetic CPGs have been demonstrated for controlling a biohybrid snake robot, where light responsive cells induce turning by stimulating neurons that control the anterior joint (Cheslet et al., 2024). Additionally, Norman-Tenazas (2021) algorithmically evaluates neuron configurations for CPGs with leaky-integrator dynamics, then applies the best performer to a snake robot with motor torque sensing for navigating peg arrays. More abstract models emphasizing CPG connectivity have been examined as well. For example, Thandiackal et al. (2021) applies Matsuoka oscillators to show that intrinsic joint oscillations, intersegmental coupling, and reflex chains sensitive to fluid forces can all drive undulation, though a combined approach is more robust. Meanwhile, Moreno and Gomez (2011) use motor primitives to adapt CPG amplitude and frequency. Combined with range sensors on the front and sides of the robot, the hierarchical structure enables the robot to avoid and climb over obstacles.

While abstract CPGs based on limit cycles have demonstrated effective control in segmented robots, some research suggests that CPGs constructed with stable heteroclinic channels (SHCs) are more responsive to sensory inputs (Horchler et al., 2015; Rabinovich et al., 2006; Shaw et al., 2015). SHCs consist of saddle equilibria connected cyclically such that the unstable manifold of one flows into the stable manifold of the next (Horchler et al., 2015). Perturbing the system away from equilibria with noise or sensor input causes state transitions, analogous to pushing a ball off of a hill Horchler et al. (2015). Perturbation intensity and timing influence residence times near equilibria (Horchler et al., 2015; Rouse et al., 2024). Ashwin and Postlethwaite (2016); Ashwin et al. (2011) describe heteroclinic cycle stability criteria with consideration to noise. Biological research on Aplysia shows that SHCs tuned for finite state machine-like transitions are responsive to sensor inputs and qualitatively reproduce *in vivo* feeding behaviors (Shaw et al., 2015). SHCs have also been applied in a simulated worm-like robot, with force sensors modulating transitions between expansion and contraction to improve locomotion through a pipe (Daltorio et al., 2013). Similarly, Brecelj and Petrič (2023b) use SHCs in a humanoid robot, where saddles correspond to stances (e.g., standing, raised hands) and forces on the grasper drive transitions. Recently, Rouse and Daltorio (2021) demonstrated that MPs based on SHCs instead of Gaussian kernels exhibit transparent control. Specifically, weights visually resemble the trajectory in a kinematic model.

Our research demonstrates movement primitives based on SHCs for control of a simulated snake robot, then assesses methods for adapting gaits by scaling and learning weight parameters, as well as incorporating sensory input. We validate the hypothesis that joint trajectories, which collectively constitute the gait, vary proportionally with SHC weight parameters. We exploit this characteristic to construct an anguilliform (eel-like) swimming gait from the lateral undulation gait. The anguilliform gait is characterized by smaller oscillations in anterior joints. We demonstrate that weights are learnable, enabling gait optimization with respect to swimming speed and efficiency. Finally, we show that gaits are enhanced by modifying the rate of progression between saddle points with sensory information. To our knowledge, this is the first work demonstrating correspondence between SHC movement primitive weights and the resulting gait in a nonlinear dynamical system.

To validate our controller, we implement both serpenoid and SHC control in a planar snake robot simulation and demonstrate that the controllers achieve comparable performance (i.e., efficiency and swimming speed) in quiescent fluid. We show that the anguiliform gait emerges by independently scaling the weight amplitudes for each joint, then characterize the relationship between weights and joint amplitudes (Figure 1). Separately, we

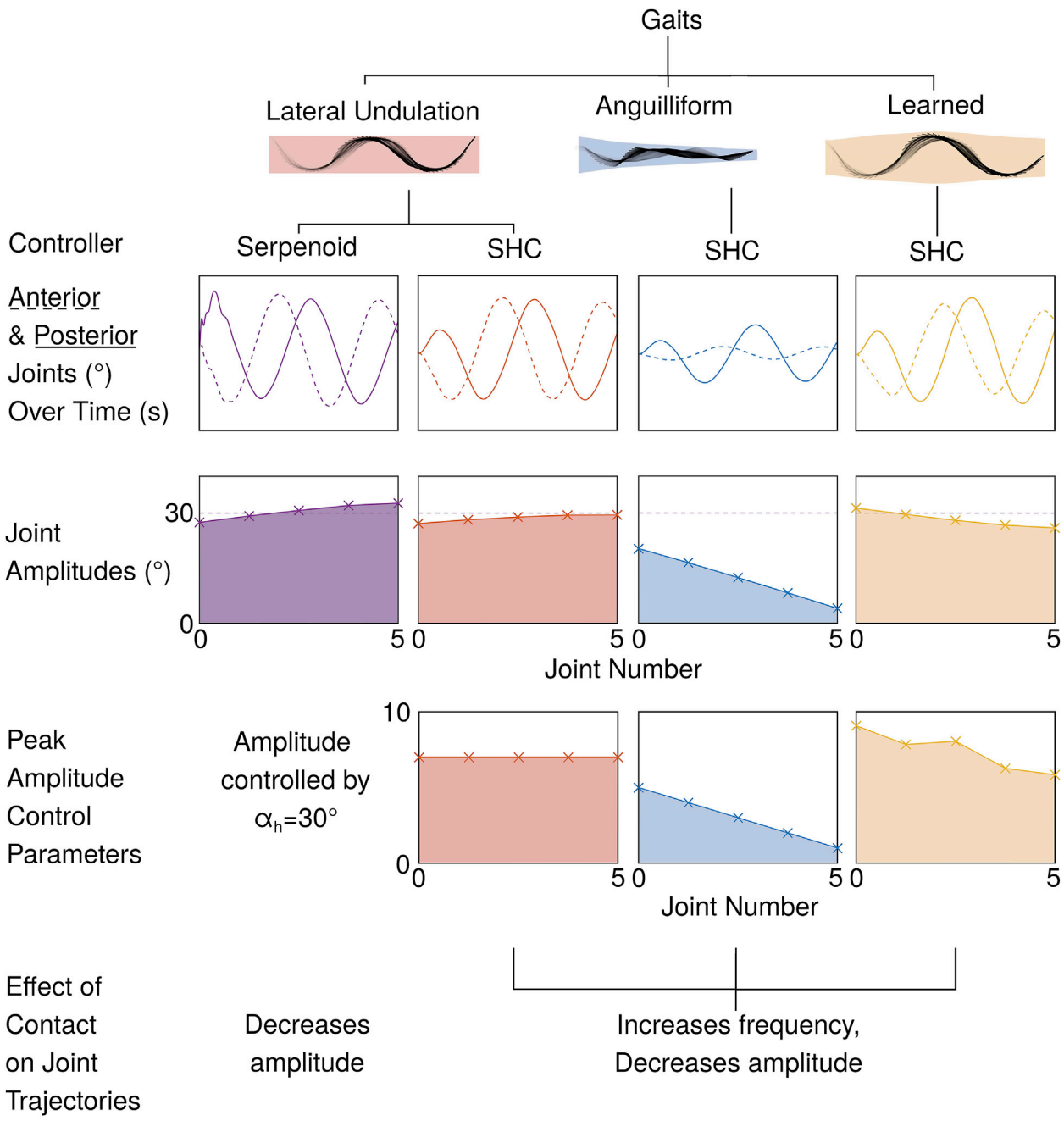

FIGURE 1
An SHC movement primitive controller, like a serpenoid controller, can realize a lateral undulation gait. With SHC movement primitives, joint amplitudes can be independently tuned by manually scaling weights, as shown by the anguilliform SHC controller. Alternatively, learning weights permits gait optimization to improve swimming speed (4 learned weights per joint; maximum weight for each joint is shown). In our SHC-based controllers, contact sensing produces a coupled change in the frequency and amplitude of the gait.

apply gradient descent to optimize the SHC weights, improving the speed of the robot in an obstacle free environment. Then we integrate tactile sensing to increase the progression rate between saddle points during contact and assess the controller performance as the robot maneuvers through both straight and uneven passages. The efficiency and speed of the simulated robot with SHC control and compliant serpenoid control are compared. Our work serves as a basis for future controllers that adapt to fluid and obstacle interactions in a biologically plausible manner.

2 Methods

2.1 Modes of locomotion

Biological snakes use various gaits for different environmental conditions. In uncluttered terrestrial environments, snakes perform lateral undulation, where a transverse wave propagates from the head to the tail (Figure 2A). All points on the body trace the same path because ground forces prevent slipping in the transverse

FIGURE 2
(A) During terrestrial lateral undulation, all joints oscillate with the same amplitude such that the lateral displacement remains the same at the front of the body as at the rear **(B)** In anguilliform locomotion, the lateral displacement is minimal near the head and increases posteriorally.

direction (Gray, 1946; Jayne, 2020). Aquatic lateral undulation, or anguilliform locomotion, is also characterized by a similar transverse wave, but the amplitude and wavelength increases from the head to the tail (Figure 2B). Different points trace distinct paths because there are no ground contact forces to facilitate nonholonomic constraints (Gray, 1946; Jayne, 2020). Instead, resistive and reactive fluid forces provide thrust (Piñeirua et al., 2015). Additionally, the muscle activation timing differs from terrestrial lateral undulation (Jayne, 2020).

In loose or slippery substrates such as sand, snakes in the Caenophidia clade switch to a sidewinding gait (Mosauer, 1932). Sidewinding is characterized by anchoring some sections of the body on the ground, thrusting the unanchored sections to one side, then repeating, alternating the unanchored and anchored sections to produce lateral locomotion. In tunnel concertina locomotion, a snake will anchor itself against both sides of a narrow passage, extend forward by straightening its joints starting from the head, then anchor itself again (Gray, 1946). A variation of concertina locomotion is also used for arboreal locomotion during climbing or along thin branches (Astley and Jayne, 2007). In spaces too narrow for concertina locomotion, snakes may use a rectilinear gait where portions of the body are lifted off the ground and moved forward, akin to walking (Lissmann, 1950).

2.2 Control

2.2.1 Lateral undulation gait with serpenoid control

In early work parameterizing snake kinematics, Shigeo (1994) proposed the serpenoid curve, wherein sinusoids approximate the shape of an undulating snake. The desired relative joint angle $\phi_i^*(t)$ for joint i at time t follows Equation 1 with joint amplitude α_h, frequency ω_h, and phase offset between joints δ_h. Biasing the relative joint angles with the steering term ϕ_0 induces whole body turning.

$$\phi_i^* = \alpha_h sin\left(\omega_h t + \delta_h (i-1)\right) + \phi_0 \tag{1}$$

Hirose's model has become popular for snake robots due to its simplicity and versatility. The serpenoid curve has been used for both terrestrial and aquatic lateral undulation (Shigeo, 1994; Ostrowski and Burdick, 1996; Sato et al., 2002; Kelasidi et al., 2014). It has also been adapted for sidewinding (Tesch et al., 2009), concertina (Chen and Roth, 2023), and rectilinear (Tesch et al., 2009) gaits. Additionally, several authors have augmented the serpenoid curve to support obstacle aided locomotion (Rollinson and Choset, 2013; Travers et al., 2018; Travers et al., 2015) and mitigate slipping (Dehghani and Mahjoob, 2009). In our work, we use it as a basis for comparison with our SHC controllers. We select gait parameters $\alpha_h = \frac{\pi}{6}$ rads, frequency $\omega_h = \frac{5\pi}{9}$ rads/s, and $\delta_h = \frac{2\pi}{9}$ rads, consistent with Kelasidi et al. (2017).

To ensure locomotion along the x axis, we adapt the steering control in Kelasidi et al. (2017). The simulated robot heading ψ is computed as the average of all linkage angles with respect to the horizontal θ (See Figure 3; Equation 2). We assign a desired heading ψ_{ref} using the steering constant $\Delta = 4l$ (where $2l$ is the length of one robot segment) and the center of mass displacement from the x axis, Y_{CM} (Equation 3). Then, the steering term ϕ_0 is computed using proportional-integral (PI) control with integral gain $k_{I,0} = \frac{0.2}{\pi}$ and proportional gain $k_{p,0} = 0.2$ (Equation 4; Table 1).

$$\psi = \frac{1}{n}\sum_{i=1}^{n}\theta_i \tag{2}$$

$$\psi_{ref} = -atan\left(\frac{Y_{CM}}{\Delta}\right) \tag{3}$$

$$\phi_0 = -k_{I,0}\int\left(\psi_{ref} - \psi\right)dt + k_{p,0}\left(\psi_{ref} - \psi\right)\Big) \tag{4}$$

The actuator torques u for each joint i are computed as in Kelasidi et al. (2014) with proportional gain $k_p = 50$, damping $k_d = 0.5$, and relative joint angles ϕ (Equation 5).

$$u_i = k_p\left(\phi_i^* - \phi_i\right) + k_d\left(\dot{\phi}_i^* - \dot{\phi}_i\right) \tag{5}$$

2.2.2 Tactile sensing with serpenoid control

Trajectory planning is enhanced by considering the interactions between the robot and environmental obstacles. Travers et al. (2015) define shape compliant control, where serpenoid curve parameters vary due to obstacle contact. Specifically, their robot senses externally applied torques on each joint and adjusts the reference joint amplitudes using an admittance controller, enabling the robot to brace against obstacles (Equation 6).

$$M_a'\left(\ddot{\alpha}_h - \ddot{\alpha}_{ref}\right) + D_a'\left(\dot{\alpha}_h - \dot{\alpha}_{ref}\right) + K_a'\left(\alpha_h - \alpha_{ref}\right) = \tau_{ext}' \tag{6}$$

In Travers et al. (2015), the admittance controller gains M_a', D_a', and K_a' are functions of the robot configuration, and the reference amplitude α_{ref} is held constant for a given joint. Their compliant control produces coordinated locomotion through an environment with regularly spaced pegs. Other methods of shape control have been explored for pipe climbing (Rollinson and Choset, 2013) and navigating rugged terrain (Travers et al., 2018).

We adopt a simplified shape controller based on Travers et al. (2015), where the robot narrows its gait by decreasing joint amplitudes during contact. Once contact ceases, the joint amplitudes return to the reference value $\alpha_{ref} = \frac{\pi}{6}$ (see Equation 7). This method reduces contact with the walls in confined spaces. We choose amplitude gain $k_\alpha = 1500$, amplitude damping $c_\alpha = 1050$, and tactile input gain $k_T = 500$. Tactile input $z_T = 1$ if any linkages contact an obstacle and $z_T = 0$ otherwise. Joints are uniformly impacted by tactile inputs from all segments.

$$\ddot{\alpha}_h + c_\alpha\left(\dot{\alpha}_h\right) + k_\alpha\left(\alpha_h - \alpha_{ref}\right) = -k_T z_T \tag{7}$$

2.2.3 Lateral undulation gait with SHC control

2.2.3.1 SHC dynamics

To validate SHC-based MPs as a viable control method snake robots, we first emulate the lateral undulation gait employed by the

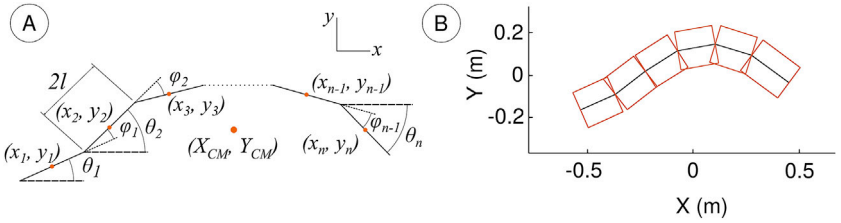

FIGURE 3
(A) Kinematic diagram of *n* segment serpentine robot. Variable naming from Kelasidi et al. (2018) **(B)** Simulated lateral undulation of a robot with $n = 6$ segments in an obstacle free aquatic environment.

TABLE 1 Serpenoid controller parameters.

Variable	Description	Value
c_α	Amplitude damping for sensorized controller $(\frac{rad}{s})$	1,050
K_u	Steering ultimate gain	1
$k_{I,0}$	Steering integral gain	$k_{p,0}/T_i = \frac{0.2}{\pi}$
$k_{p,0}$	Steering proportional gain	$0.2K_u = 0.2$
T_i	Steering integral period	$0.5T_u = \pi$
T_u	Steering ultimate period	2π
δ_h	Angular offset between joints	$\frac{2\pi}{9}$
k_α	Amplitude proportional gain for controller with tactile sensing	1,500
k_T	Proportional gain for contact disturbances	500
α_0	Equilibrium amplitude (rad)	$\frac{\pi}{6}$
α_h	Amplitude (rad)	$\frac{\pi}{6}$
β_h	Frequency (rad/s)	$\frac{5\pi}{9}$

serpenoid controller. SHCs encode rhythmic behavior as cyclic progression between saddle points or kernels. The kernel activity $x_{1\times K}$, which denotes proximity to each of the K saddle points, is given by Equation 8 (Rouse and Daltorio, 2021; Daltorio et al., 2013). The $\odot$ operator indicates element-wise multiplication. The kernel activity dictates the phase of the rhythmic trajectory. Oscillation of all joints is established by generating two cycles in antiphase, one for counterclockwise and one for clockwise motion. Counterclockwise and clockwise motor commands are analogous to contraction of muscles on the left and right side of a biological snake. Maintaining distinct cycles for each direction allows phase differences between joints to be easily defined and emphasizes how couplings between joints can drive undulation. Connections between counterclockwise and clockwise components should be included in future research, similar to other works (Norman-Tenazas, 2021; Wang Z. et al., 2017).

With a phase offset of $\frac{2\pi}{9}$ radians between joints and separate kernels for each direction, it is convenient to choose $K = 18$ kernels.

$$\tau dx = x \odot (\alpha^T - x\rho)dt + \eta dW_x \tag{8}$$

Considering only the subformula $\tau dx = (x \odot \alpha^T)dt$, the activity of the i^{th} kernel grows exponentially according to its growth rate, α_i and the time scaling factor $\tau = 1$. Then, we design an inhibition matrix $\rho_{K\times K}$ such that each kernel inhibits itself and all other kernels in the same cycle except the next one in the sequence. The inhibition causes kernels to momentarily activate $(x_i > 0.9)$ in a winnerless competition (Horchler et al., 2015). To ensure stability, the kernel activity is bounded such that $0.0005 \le x \le 1$, as in Rouse and Daltorio (2024). Since the proposed SHC controller includes one cycle corresponding to counterclockwise and another for clockwise motion of each joint, we compose the relationship between kernels using a block diagonal connection submatrix $\rho^s_{\frac{K}{2}\times\frac{K}{2}}$ as in Equations 9, 10.

We refer to Rouse and Daltorio (2024) as a guideline for tuning the SHC MP controller. The study outlines how inhibition parameters impact kernel activation and trajectories as the controller traces a square. The growth rate α influences how quickly the kernels are excited, thereby influencing the frequency of the CPG. The growth magnitude β controls the peak amplitude of kernels. When $\beta < 1$, the kernel and trajectory amplitude are reduced. For $\beta > 1$, kernels maintain their maximum activity $x_i = 1$ for an extended period, then decay slowly. The resulting trajectory has increased amplitude, slower transitions away from each vertex, and a phase shift. The insensitivity to noise ν determines how likely perturbations are to induce state transitions. Varying $\nu < 1$ has little

TABLE 2 SHC controller parameters.

Variable	Description	Value
K	Number of kernels	18
K_u	Steering ultimate gain	2
K_p	Steering proportional gain	$0.2K_u = 0.4$
k_t	Tactile sensing gain	0.55
P	Steering gain matrix	$([K_p/T_i, K_p, K_pT_d]^T 1_{1\times K})^T$
T_d	Steering derivative period	$0.333T_u = 0.333$
T_i	Steering integral period	$0.5T_u = 0.5$
T_u	Steering ultimate period	1
x	Kernel Activation	$[0.0004, 1]$
$x_{t=0}$	Initial conditions of kernels	$[0.0093, 0.9756, 0_{1\times6}, 0.0093, 0_{1\times5}, 0.45, 0.5, 0, 0]$
z_t	Tactile sensing signal	1 if contact, 0 otherwise
α	Growth rate	23.2
α_ϕ	Damping coefficient	4
β	Magnitude	1
β_ϕ	Proportional gain coefficient	1
η	Noise magnitude	$1 \times 10^{-9} \cdot 1_{K\times n_{sensors}}$
λ_{1-4}	Weight parameter	$[3, 7, 3, 7]$ (Lateral undulation SHC only)
ϕ_{goal}	Joint trajectory goal	0
ν	Insensitivity to noise	1
τ	Temporal scaling factor	1

impact on the kernel activation or trajectories. Increasing ν above 1 allows more precision near waypoints, but distorts transitions between waypoints and reduces the frequency of the cycle. We select the growth rate for all joints $\alpha = 23.2$ such that the overall frequency of the CPG is the same as the frequency of the serpenoid controller ω_h. To avoid distorting the shape or frequency of the lateral undulation gait, we set $\beta = 1$ and $\nu = 1$.

$$\rho^s_{i,j} = \begin{cases} \alpha_i/\beta_i & if\ i = j \\ \dfrac{\alpha_i - \alpha_i/\nu_i}{\beta_j} & if\ i = j \oplus 1 \\ \dfrac{\alpha_i + \alpha_j}{\beta_j} & otherwise \end{cases} \tag{9}$$

$$\rho = \begin{bmatrix} \rho^s & 0 \\ 0 & \rho^s \end{bmatrix} \tag{10}$$

In addition to the excitatory and inhibitory components, the heteroclinic dynamics are augmented with Brownian noise via a time invariant Wiener process, W_x (Equation 8) (Daltorio et al., 2013; Ashwin and Postlethwaite, 2016; Shaw et al., 2015). Using Euler-Maruyama integration, the noise term is represented as $\eta dW_x = \eta\sqrt{dt}\mathcal{N}(0, 1)$, where $\eta = 10^{-10}$ is a scaling parameter, $dt = 0.001\,s$ is the simulation time step, and $\mathcal{N}_{1\times K}(0, 1)$ is a vector of normally distributed noise with mean of 0 and standard deviation of 1. The chosen scaling parameter is within ranges used in prior works (Horchler et al., 2015; Rouse and Daltorio, 2024; Daltorio et al., 2013) and is large enough to ensure sustained, regular transitions without causing the kernel activity to appear noisy. Though stability analysis for our controller with respect to noise (see Ashwin et al., 2011) would be valuable, this is left to future work. Parameter values are listed in Table 2.

2.2.3.2 Movement primitives with SHCs

To integrate SHCs with the MP framework, we define the desired joint accelerations $\ddot{\phi}^\star$ as a function of kernel activity and current joint configuration (Equation 11). From the accelerations, desired joint velocities and angles are derived via explicit Euler integration.

$$\ddot{\phi}^\star = \alpha_\phi\left(\beta_\phi\left(\phi_{goal} - \phi^\star\right) - \dot{\phi}^\star\right) + f(x) \tag{11}$$

The first term constitutes a PD controller with gain parameters $\alpha_\phi = 4$ and $\beta_\phi = 1$ [consistent with Rouse and Daltorio (2021), Rouse and Daltorio (2024)] to ensure reference tracking. We choose an equilibrium joint angle $\phi_{goal} = 0$ such that the robot progresses in a straight line. The mapping function $f(x)$ in Equation 11 dictates the shape of the trajectory. We adapt the mapping function defined in Rouse and Daltorio (2021) (Equation 12).

$$f(x) = \frac{x\left(w^T + P\left(z_{ref} - z\right)\right)}{\sum_{i=1}^{K} x_i} \tag{12}$$

The weight matrix $w_{n-1\times K}$ defines the sensitivity of the joints to the activity of each kernel. We also incorporate Proportional Integral Derivative (PID) steering control with gain matrix $P_{K\times 3} = 1_{K\times 1}[0.8, 0.4, 0.133]$, reference signal $z_{ref} = [\psi_{ref}, \dot{\psi}_{ref}, \ddot{\psi}_{ref}]$, and heading parameters $z = [\psi, \dot{\psi}, \ddot{\psi}]$. The steering gains are tuned with a Ziegler-Nichols closed loop method adjusted for no overshoot (McCormack and Godfrey, 1998). The forcing term is normalized by the total kernel activity.

The weight submatrix $w_{n-1\times\frac{K}{2}}$ is chosen according to Equation 13 and the overall weights are assigned as in Equation 14. The operators $\oplus$ and $\ominus$ indicate circulant addition and subtraction, respectively. We assign $\lambda_1 = \lambda_2 = 3$ and $\lambda_3 = \lambda_4 = 7$. The weight matrix encodes the positive (counterclockwise) and negative (clockwise) trends in joint angles as the corresponding kernels become active or inactive.

$$w^s_{i,j} = \begin{cases} \lambda_1 & if\ i = j \oplus 1 \\ \lambda_2 & if\ i = j \ominus 2 \\ \lambda_3 & if\ i = j \\ \lambda_4 & if\ i = j \ominus 1 \\ 0 & otherwise \end{cases} \tag{13}$$

$$w = [w^s, -w^s] \tag{14}$$

Once the desired joint accelerations, velocities, and positions are computed for a given time step, we evaluate the joint torques using the same methods as in Equation 5 in Section 2.2.1.

2.2.4 Anguilliform gait with SHC control

Replicating the anguilliform gait with SHC control provides an opportunity to assess the scalability of SHC movement primitive trajectories. In Rouse and Daltorio (2021), the authors demonstrate that weight parameters for SHC movement primitives visually represent and are proportional to the desired trajectory for a simple kinematic model. Inspired by their work, we examine how gaits can be adapted by scaling the weights. Specifically, we assess weight scaling as a means of switching from the terrestrial lateral undulation gait to anguilliform locomotion. Kelasidi et al. (2014) approximate anguilliform locomotion by linearly scaling the joint amplitudes in their serpenoid controller as in Equations 15, 16.

$$g(i,n) = \frac{n-i}{n+1} \tag{15}$$

$$\phi^*_i = \alpha_h g(i,n) sin(\omega_h t + \delta_h (i-1)) + \phi_0 \tag{16}$$

to implement an anguilliform gait with SHC control, we apply the scaling relationship in Equation 15 to the weight matrix (Equation 17). We expect that scaling the weights will proportionally change the amplitude of the trajectories for each joint.

$$w^a_{i,j} = w_{i,j} g(i,n) \tag{17}$$

2.2.5 SHC control with tactile sensing

CPGs, both in biological systems and robots, are most useful when they can be adapted by sensory information. Here, we establish a mechanism for incorporating tactile signals into SHC movement primitives, with the goal of improving speed of the simulated snake robot as it undulates through confined spaces. We introduce the term $k_T z_T$ into the SHC canonical state equation, where $k_T = 0.55$ (Equation18). We assign $z_T = 1$ if any linkage contacts an obstacle and $z_T = 0$ otherwise, as in Section 2.2.2. During contact, kernels progress more quickly such that joints have less time to accelerate and joint amplitudes decline. The increased kernel progression rate also increases joint oscillation frequency, leading to higher thrust (Huang et al., 2019) that may enable the robot to overcome friction if contact persists. Since all tactile sensors affect every kernel, phase differences between joints remain constant and coordinated locomotion is maintained. In future work, we may consider alternative SHC formulations that allow tactile sensors to impact joints independently.

$$\tau dx = x(1 + k_T z_T)(\alpha^T - x\rho)dt + \left(\eta\sqrt{dt}\,\mathcal{N}(0,1)\right)^T \tag{18}$$

2.2.6 Learned gait with SHC control

Robots, like animals, benefit from optimizing the speed and energy efficiency of locomotion. In (Rouse and Daltorio, 2021), the authors demonstrate that weights in SHC movement primitives can be learned to replicate a known trajectory for a purely kinematic system. Here, we extend their work, improving the robot's performance by adjusting weights with consideration to the system dynamics. Beginning with the SHC controller for lateral undulation (see Section 2.2.5), we simulate swimming for $t_{max} = 10$ seconds in an obstacle-free environment. The forward velocity of the center of mass (Equation 19) and energy efficiency of locomotion are assessed. We define efficiency as the overall cost of transport (COT) (Equation 20), where $t_{start} = 0$s, $G = 9.81\frac{m}{s^2}$ is the acceleration due to gravity and m_{total} is the total mass of the robot.

$$v_{avg} = \frac{1}{t_{max}} \sum_{t=t_{start}}^{t_{max}} \left(\dot{X}_{CM} dt\right)_t \tag{19}$$

$$COT = \frac{\sum_{t=t_{start}}^{t_{max}} \sum_{i=1}^{N_{joints}} \left|u_{i,t}\dot{\phi}_{i,t}\right|}{G m_{total} X_{CM}(t_{max})} \tag{20}$$

We establish a cost function (Equation 21) rewarding velocity, while penalizing poor efficiency. Note that the velocity is larger than the COT for lateral undulation such that this cost function prioritizes speed.

$$cost = 5000\|COT\| - 5000 v_{avg} \tag{21}$$

we numerically approximate the gradient of the cost function with respect to $\lambda_{1-4,i}$ for each joint i. The weights are improved via gradient descent with a learning rate $\eta_{learn} = 0.01$ until the rate of change of weights $d\lambda_{1-4,i} \leq 0.01$, requiring 155 iterations (Equation 22). The selected learning rate allows smooth improvement in performance, and changes become relatively small by the time the stop condition is reached (see Supplementary Figure). While our experiments in Sections 2.3.2, 2.3.3 include obstacles, the weights are not relearned for these conditions. The tactile sensing parameters are kept the same as in Section 2.2.5.

$$w = w - \eta_{learn} \cdot \nabla cost(w) \tag{22}$$

TABLE 3 Parameters for fluid dynamics, obstacle modeling, and kinematics.

Variable	Description	Value
C_A	Added mass coefficient	1
C_D	Drag coefficient perpendicular to link axis	2
C_f	Drag coefficient along link axis	0.03
C_M	Added inertia coefficient	1
c_{wall}	Obstacle damping coefficient $(N \cdot s/m)$	500
dt	Simulation time step (s)	0.001
$dx_{segment}$	Point resolution for collision dynamics (m)	0.01
dx_{wall}	Feature width for obstacles (m)	0.001
e_1	major radius (m)	0.09
e_2	minor radius (m)	0.035
F_C	Sliding friction (N)	—
F_N	Normal force (N)	—
F_S	Static friction (N)	—
G	Gravitational acceleration $(\frac{m}{s^2})$	9.81
k_d	Motor derivative gain	0.5
k_p	Motor proportional gain	50
k_{wall}	Obstacle stiffness coefficient (N/m)	30,000
l	link half-length (m)	$[0.09_{1\times5}, 0.11]$
m	link mass (kg)	$[0.5_{1\times5}, 0.94]$
n	Number of links	6
u	Joint torque $(N \cdot m)$	—
$\theta(t)$	Absolute angle of linkages (rad)	—
μ_k	Coefficient of kinetic friction	0.6
μ_s	Coefficient of static friction	0.8
$\phi(t)$	Relative joint angles (rad)	—
$\phi^*(t)$	Desired relative joint angles (rad)	—
ρ_f	Fluid density (kg/m^3)	1,000
ψ	Robot heading (rad)	—

2.3 Experimental design

2.3.1 Obstacle-free swimming

We first consider a simulated robot quiescent water with no obstacles. We adopt the framework proposed by Kelasidi et al. (2017), which addresses a submerged planar robot comprised of discrete linkages with elliptical cross sections. Fluid is viscous, incompressible, and irrotational in the reference frame of the robot. The authors develop equations of motion for the center of mass (X_{CM}, Y_{XM}) and linkage orientation θ including linear drag, nonlinear drag, and added mass in an unobstructed environment. Relative joint angles are derived from kinematics as $\phi_i = \theta_{i+1} - \theta_i$. We consider a robot with $n = 6$ segments, where each segment has a major radius $e_1 = 0.09m$, minor radius $e_2 = 0.035m$, half-length of $l = 0.09\,m$, and a mass of $m = 0.5\,kg$, except the head segment. The head segment is extended ($l_6 = 0.11\,m$ and $m_6 = 0.94\,kg$) to accommodate electronic components for a physical robot, which is under development. Fluid parameters and fluid body interaction constants are kept consistent with Kelasidi et al. (2017) (fluid density $\rho_{fluid} = 1000\,kg/m^3$, added mass coefficient $C_A = 1$, added inertia coefficient $C_M = 1$, drag coefficient along link axis $C_f = 0.03$, and drag coefficient perpendicular to link $C_D = 2$). All simulation parameters can be found in Table 3.

The experiment is conducted for the serpenoid, lateral undulation SHC, anguilliform SHC, and learned SHC controllers. The simulation runs for 60 s, recording the robot's position, joint torques, and joint velocities. Power consumption is approximated as $P_t = \sum_{i=1}^{n-1} |u_{i,t}\dot{\phi}_{i,t}|$. Then, we compare the swimming speed and COT for each controller. Additionally, we assess the differences in behavior for SHC controllers by examining the joint trajectories, kernel activity, and forcing term $f(x)$. At time $t = 0$, the robot is at rest with all linkage angles $\theta_i = 0$ and the center of mass located at the origin.

2.3.2 Straight channels

Simulating the robot in structured environments allows us to assess our method for integrating tactile information with SHC control. We examine straight passages ranging from $W = 0.2\,m$ to $W = 0.7\,m$ in width, at intervals of $0.01\,m$. The minimum width allows $0.01\,m$ of freedom on each side of the robot, while the maximum channel width permits the joints to oscillate freely if the robot is centered. The robot begins entirely in the channel with $\theta_i = 0$ and no contact with the walls. The overall COT and average velocity are calculated after 30 s of swimming for each case. This experiment addresses the serpenoid and lateral undulation SHC without sensing, as well as the serpenoid, lateral undulation SHC, and learned SHC with tactile sensing (+T).

Obstacles are treated as points connected by flat surfaces with stiffness $k_{wall} = 30,000\frac{N}{m}$ and damping $c_{wall} = 500\frac{N}{m \cdot s}$. We approximate each robot segment as a set of points spaced $dx_{segment} = 0.001\,m$ apart and assume that points colliding with an obstacle penetrated the nearest surface. The normal distance d_N and normal velocity v_N between the point and surface are computed, then the normal force centered at the point is approximated as $F_N = (k_{wall} \cdot d_N + c_{wall} \cdot v_N) \cdot dx_{segment}$. We incorporate friction via a linear model with stiction (Marques et al., 2016), where $F_S = \mu_s F_N$, $F_C = \mu_k F_N$, $\mu_s = 0.8$, and $\mu_k = 0.6$. The details are replicated in Equation 23. The variables v_T, $v_0 = 0.001\frac{m}{s}$, and $v_1 = 0.002\frac{m}{s}$ represent the tangential velocity, velocity at maximum static friction, and velocity at which only kinetic friction occurs (Table 3). Torque is obtained by integrating contact forces over the displacement from the link center of mass. The effects of obstacles on fluid behavior are ignored for simplicity, and fluid far from the robot remains quiescent.

$$\mathbf{F_f} = \begin{cases} \left(\frac{\|\mathbf{v}_T\|}{v_0} F_S\right) \mathrm{sgn}(\mathbf{v}_T) & \text{if } \|\mathbf{v}_T\| \le v_0 \\ \left(F_S - \frac{\|\mathbf{v}_T\| - v_0}{v_1 - v_0}(F_S - F_C)\right) \mathrm{sgn}(\mathbf{v}_T) & \text{if } v_0 < \|\mathbf{v}_T\| < v_1 \\ F_C \mathrm{sgn}(\mathbf{v}_T) & \text{if } \|\mathbf{v}_T\| \ge v_1 \end{cases} \tag{23}$$

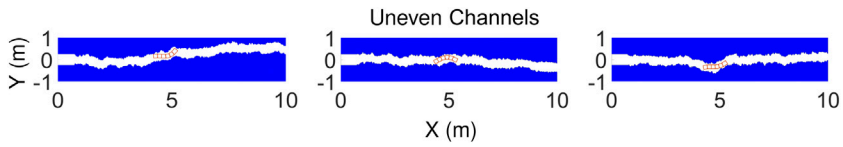

FIGURE 4
Examples of uneven channels with randomly generated features that impede the robot.

2.3.3 Uneven channels

One of the most daunting aspects for exploratory robots is maintaining productive locomotion in complex terrain. We simulate the robot moving through channels with randomly generated feature (see examples in Figure 4). To establish consistent initial conditions, each channel begins with a $1.5m$ long and $0.5m$ wide straight section. The robot begins completely straight, at rest, and inside the channel. After the straight section, the upper surface of the channel is constructed such that $x_{wall,i} = x_{wall,i-1} + 0.025$ and $y_{upper,i} = y_{upper,i-1} + \mathcal{N}(\mu = 0, \sigma = 0.03)$. Points along the bottom surface $y_{lower,i}$ are computed likewise. If the distance between $y_{upper,i}$ or $y_{lower,i}$ and any point on the opposite boundary is less than the minimum channel width $W_{min} = 0.30m$ (1.7 times robot width), the i^{th} upper and lower points are replaced. Similarly, the i^{th} points are regenerated if the distance between $y_{upper,i}$ and $y_{lower,i}$ exceeds $W_{max} = 0.5m$ (2.8 times robot width) apart so that results do not simply reflect obstacle-free behavior. Due to random walk, the center lines shift laterally up to 1.6–3.0 robot widths over a single length of the robot, depending on the channel.

We simulate 60 s of swimming in each channel using the serpenoid and lateral undulation SHC controllers with and without tactile sensing. The learned SHC controller (+T) is also examined. Steering is disabled since the direction of the channel varies. We estimate the minimum number of channels required $n_{channels,min} = 61$ using power analysis conducted in the software G*Power for 1-way ANOVA with effect size $f_p = 0.25$, power $\alpha_p = 0.95$, and five groups. To account for invalid results, we increase the sample size to $n_{channels} = 65$. Specifically, data is excluded if the robot does not enter and remain within the uneven portion of the channel. We compute the COT and velocity using only time steps after the robot has fully entered the uneven section. Since the data does not follow normality assumptions, we assess statistical significance with Kruskal–Wallis testing, followed by Dunn-Šídák *post hoc* analysis. Furthermore we categorize the progress for each controller as continual, ceased, or intermittent. We specify that progress has ceased if the robot does not move forward by more than 0.1 m for at least 7.2 s (two gait cycles under unimpeded locomotion). We define intermittent progress where forward motion ceases for at least two gait cycles, but later resumes. The rates of continual, ceased, and intermittent progression for each controller are assessed.

3 Results

3.1 Obstacle-free swimming

3.1.1 Lateral undulation gait with SHC control

In quiescent fluid with no obstacles, the SHC controller successfully replicates the lateral undulation gait. The SHC controller produces similar joint oscillations to the serpenoid controller, but with a smoother transition from rest to steady state oscillation (Figure 5A). For both methods, the heading naturally oscillates during undulation. The steering controllers compensate by increasing or decreasing the desired joint trajectories, causing joint amplitudes to differ from the reference value of $\alpha_h = 30°$.

Since the serpenoid and lateral undulation SHC controllers generate similar trajectories, they achieve comparable performance. The average velocity of the center of mass for both controllers is $v_{avg,serpenoid} \approx v_{avg,LUSHC} = 0.28\frac{m}{s}$. The progression of the robot for all controllers is depicted in Figure 5 (also see Supplementary Files for Supplementary Video recording). (B) Due to differences in steering controller implementations, the SHC controller produces slightly better steady state efficiency ($COT_{t_{start}=1,LUSHC} = 0.087$) than the serpenoid controller ($COT_{t_{start}=1,serpenoid} = 0.097$) (Table 4).

A benefit of SHC control over serpenoid control is apparent when assessing the overall COT including transient effects ($t_{start} = 0$). The conventional serpenoid curve yields a desired trajectory with nonzero initial joint angles and velocities, whereas most robots realistically start from rest. High accelerations, large joint torques, and high energy consumption are required to reduce the trajectory error, leading to an overall COT of 0.126 (30% above steady state value). Shape-based control of the joint amplitude avoids this issue, albeit at increased complexity (Travers et al., 2015; 2018; Rollinson and Choset, 2013). In contrast, the SHC framework natively computes desired accelerations, then the desired velocity and position are evaluated by integration. This yields smooth kinematic trajectories such that the lateral undulation SHC controller achieves an overall COT only 1% greater than its steady state value (Figure 5A).

3.1.2 Anguilliform gait with SHC control

By linearly scaling the SHC weights, we transform the lateral undulation gait to an anguilliform gait, with reduced anterior joint amplitudes. For example, we scale the weights for the anterior-most joint by $g_5 = 14\%$ (Equation 15) relative to weights for the lateral undulation SHC controller. Consequently, the anguilliform SHC controller forcing term $f_5(x)$ magnitude is lower in comparison with the lateral undulation SHC (Figure 6A). This translates to a smaller joint amplitude (Figure 6C). The lateral undulation SHC controller exhibits a joint amplitude of 29.5°, while the anguilliform SHC controller's anterior joint amplitude reduces to 4.0° (13.6%), showing good correspondence with the scaling factor g_5.

Scaling effects are more thoroughly characterized by considering the amplitudes of weights and ϕ for all joints (Figures 6B, D). The SHC weight amplitude for joint j is defined by the maximum value

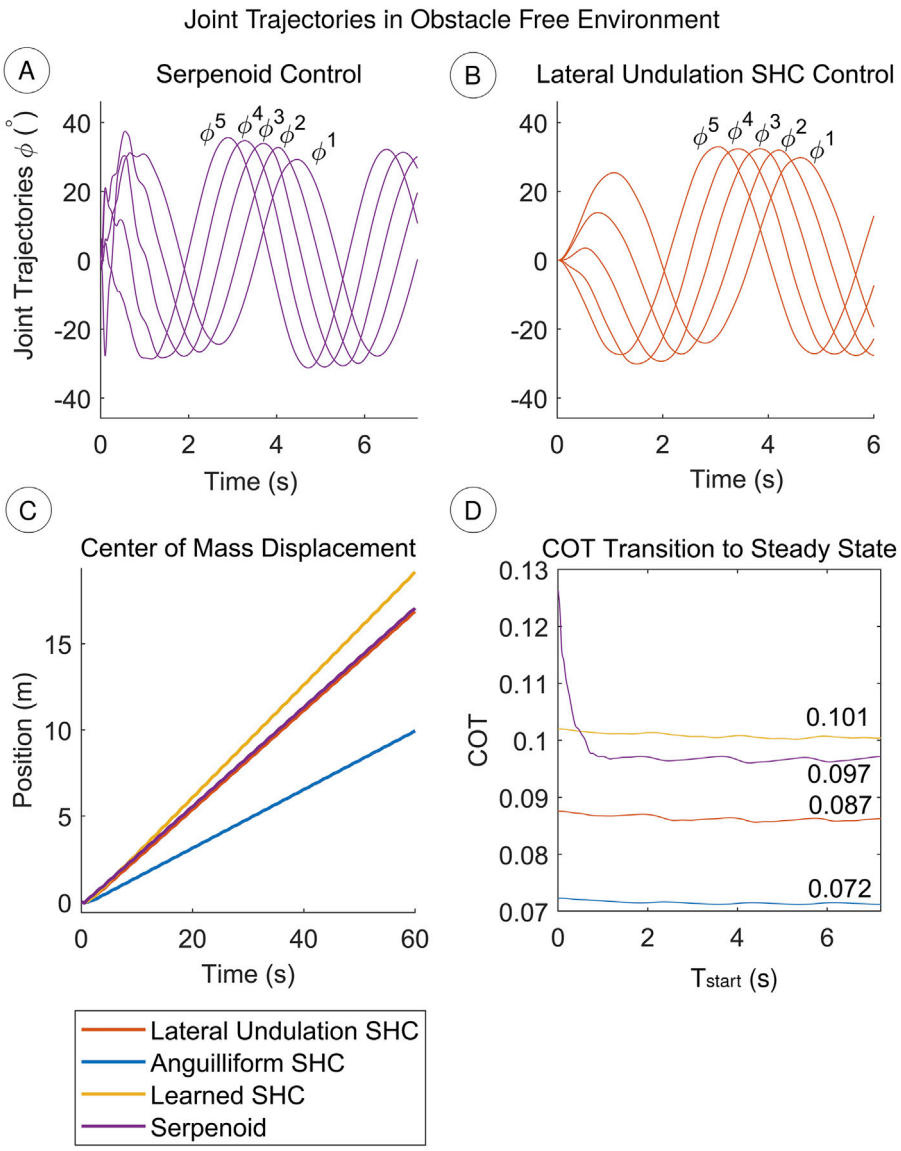

FIGURE 5
(A, B) The SHC controller produces comparable trajectories to the serpenoid controller **(C)** In obstacle-free conditions, the lateral undulation SHC performs similarly to the serpenoid controller. The anguilliform SHC controller swims slower because the joint oscillation amplitude is reduced, so thrust decreases. Learning SHC weights improves speed. Video is included in Supplementary Files **(D)** The COT reaches steady state performance after $t_{start} = 1s$ for all controllers. Due to nonsmooth trajectories, the serpenoid controller experiences higher transient energy losses and larger overall COT (i.e., COT at $t_{start} = 0$) than SHC controllers.

TABLE 4 Performance during obstacle-free swimming.

Controller	Average velocity (m/s)	Overall COT	COT after t = 1 s
Lateral Undulation SHC	0.281	0.088	0.087
Anguilliform SHC	0.166	0.072	0.072
Learned SHC	0.319	0.102	0.101
Serpenoid	0.284	0.126	0.097

in the j^{th} row of the weight matrix (Figure 7). Anguilliform SHC weight amplitudes decrease linearly from the tail to the head, with similar trends emerging in joint amplitudes. The visible correspondence between weights, forcing term $f(x)$, and joint trajectories makes SHC MPs a transparent framework that robot operators can intuitively modify. Because lateral displacement is

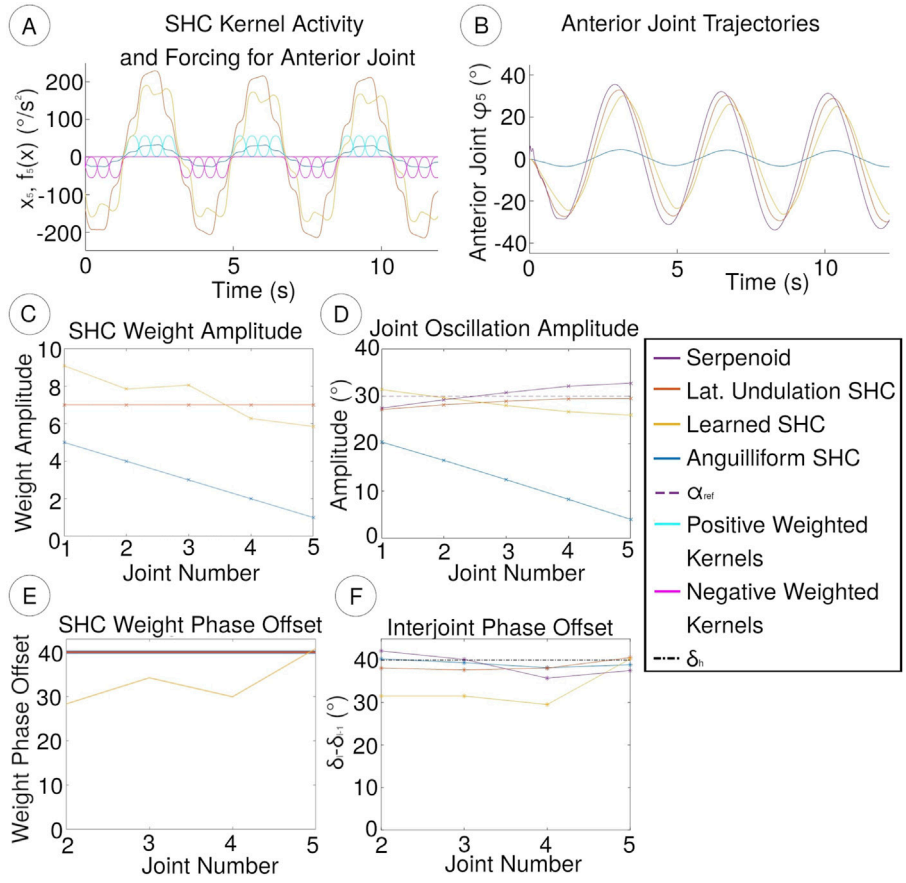

FIGURE 6
(A) Positively (cyan) and negatively (magenta) weighted SHC kernels x for the anterior joint activate in alternatingly, encoding upward and downward trends in the forcing term $f_5(x)$. Lower weights cause smaller oscillations for the anguilliform SHC controller **(B)** Anterior joint trajectories resemble SHC forcing terms. Reduced $f_5(x)$ for the anguilliform SHC controller corresponds to small anterior joint oscillations **(C)** The lateral undulation SHC controller uses the same weights for all joints. Anguilliform controller weights are scaled linearly with lower magnitudes for anterior joints. Learning yields a similar trend **(D)** Lateral undulation SHC and serpenoid controllers joint amplitudes differ slightly from the desired value α_h due to steering and fluid effects. SHC joint amplitude trends resemble the weight amplitude trends **(E)** For lateral undulation and anguilliform SHC controllers, the peak weights are consistently 40° apart. The learned SHC controller develops smaller phase offsets near 30° **(F)** In the learned SHC gait, phase offsets between joints are reduced except in the anterior joint, corresponding to shifts in weights.

reduced, the anguilliform gait produces less thrust and slower swimming ($0.166\frac{m}{s}$) than the lateral undulation gait. However, the anguilliform gait is more efficient by 26.1% ($COT = 0.0718$) relative to serpenoid control ($COT = 0.0972$) and 17% relative to lateral undulation SHC control ($COT = 0.0867$). While we only simulate one sample and recommend more comprehensive experiments with hardware, results qualitatively agree with prior work showing that efficiency is optimized at lower amplitudes compared to velocity (Anastasiadis et al., 2023).

3.1.3 Learned gait with SHC control

Our gait optimization for SHC control modifies the weight parameters to enhance speed of locomotion, while minimally affecting energy efficiency. The learned SHC controller achieves a 12.3% higher overall velocity ($0.32\,m/s$) compared with the lateral undulation SHC controller. The steady state efficiency degrades, with the COT increasing from 0.087 in the lateral undulation gait to 0.10 in the learned gait.

The improved speed of locomotion in the learned SHC controller corresponds to changes in the controller weights and joint amplitudes. Relative to the lateral undulation SHC controller, the learned SHC controller possesses higher weight amplitudes for the posterior joints and lower weights for the anterior joints (7 (B)). The learned SHC weight amplitudes correspond loosely to the joint amplitudes (Figure 6D), which show a gradual decrease towards the head of the robot. Compared with anguilliform and lateral undulation SHC controllers, the learned controller shows weaker correspondence between weights and joint amplitudes because the distribution of weights, and thus acceleration patterns, may differ between joints.

When optimizing weight parameters for the learned SHC controller, the distribution of weights for each joint changes along with the peak amplitude. We compute the phases of weight distributions δ_j^w for each of the j joints using a centroid method (Equations 24–27).

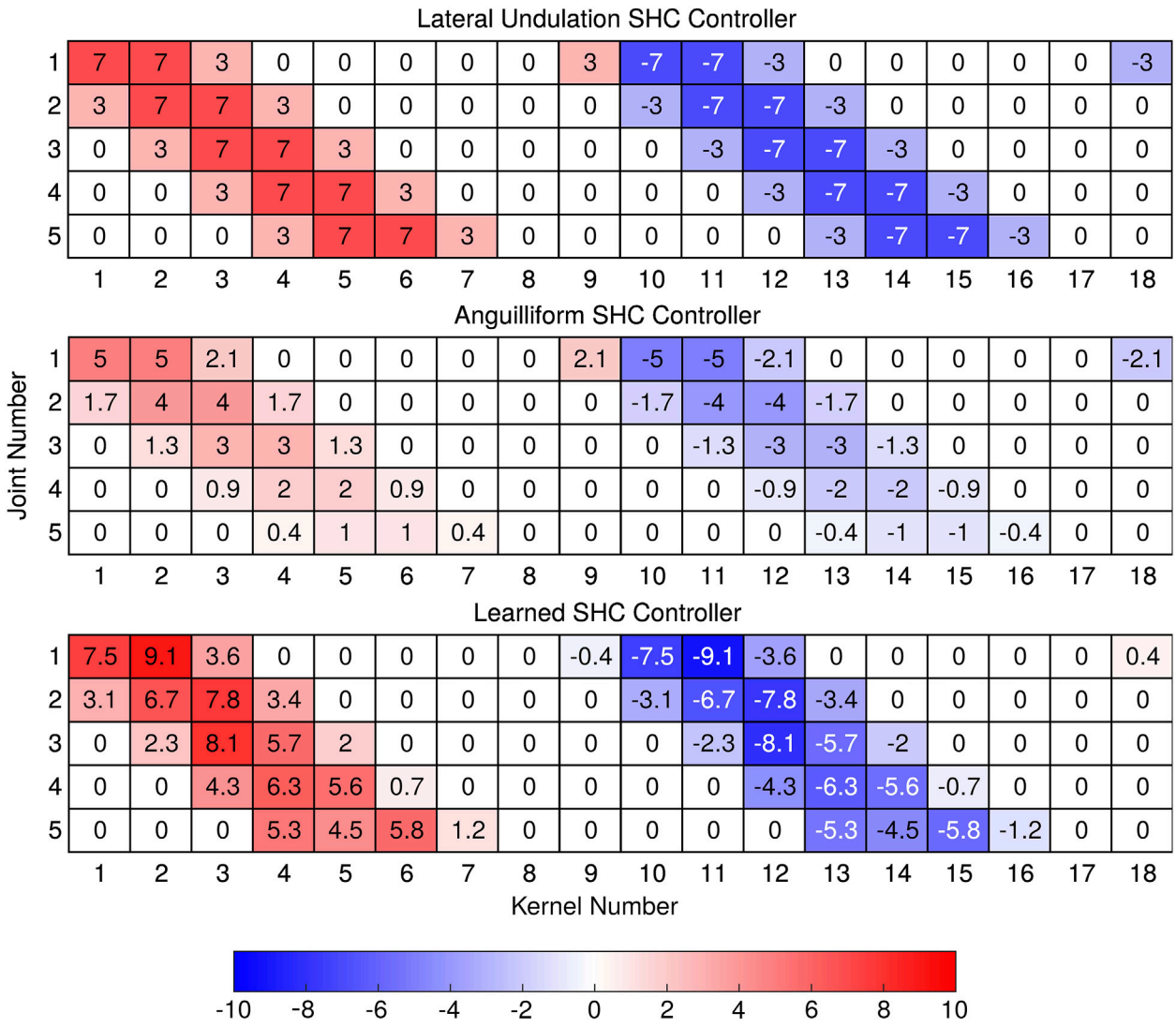

FIGURE 7
Weights for SHC controllers. Lateral undulation uses consistent weights across all joints, while the anguilliform weights decrease in magnitude from the tail (joint 1) to the head (joint 5). In the learned gait, peak weights also decrease towards the head, although the phase differences between joints also differ because $\lambda_{1-4,i}$ are tuned independently for joint i.

$$\delta_{j,k} = \frac{360\,(k-1)}{\frac{K}{2}}, \quad 1 \le k \le \frac{K}{2} \tag{24}$$

$$x_j^w = \frac{\sum_{k=1}^{K/2} w_{j,k} cos\left(\delta_{j,k}\right)}{\sum_{k=1}^{K/2} w_{j,k}} \tag{25}$$

$$y_j^w = \frac{\sum_{k=1}^{K/2} w_{j,k} sin\left(\delta_{j,k}\right)}{\sum_{k=1}^{K/2} w_{j,k}} \tag{26}$$

$$\delta_j^w = atan\left(\frac{y_j^w}{x_j^w}\right) \tag{27}$$

Gait optimization produces weight phase offsets between joints $\Delta\delta_j^w = \delta_j^w - \delta_{j-1}^w$ mostly near 30°, lower than the design value of $\delta_h = 40°$ applied for other controllers (Figure 6E). The phase offset for the anterior joint pair may differ due to the longer segment length and increased mass, or because the $\Delta\delta_5^w$ has little impact on the optimization cost function. For all controllers, the weight phase offsets identified in the weight matrix are good predictors for phase offsets in the joint trajectories $\Delta\delta_j = \delta_j - \delta_{j-1}$ (Figure 6F). Some deviation occurs due to steering and fluid effects in all controllers.

3.2 Straight channels

We assess our method for integrating sensory information in the SHC controller by examining the robot's progress through straight, narrow passages. Video of the robot in a $0.3m$ channel is included in Supplementary Files. In cases where the robot penetrates deeply into obstacles, frictional forces are overestimated such that the robot slows abruptly. In future work, this can be resolved with smaller time steps during contact. Nevertheless, controllers that incorporate tactile information (denoted by (+T)) adapt their behavior to accommodate contact, enabling forward locomotion (Figure 8B). In contrast, unsensorized controllers push backwards against the

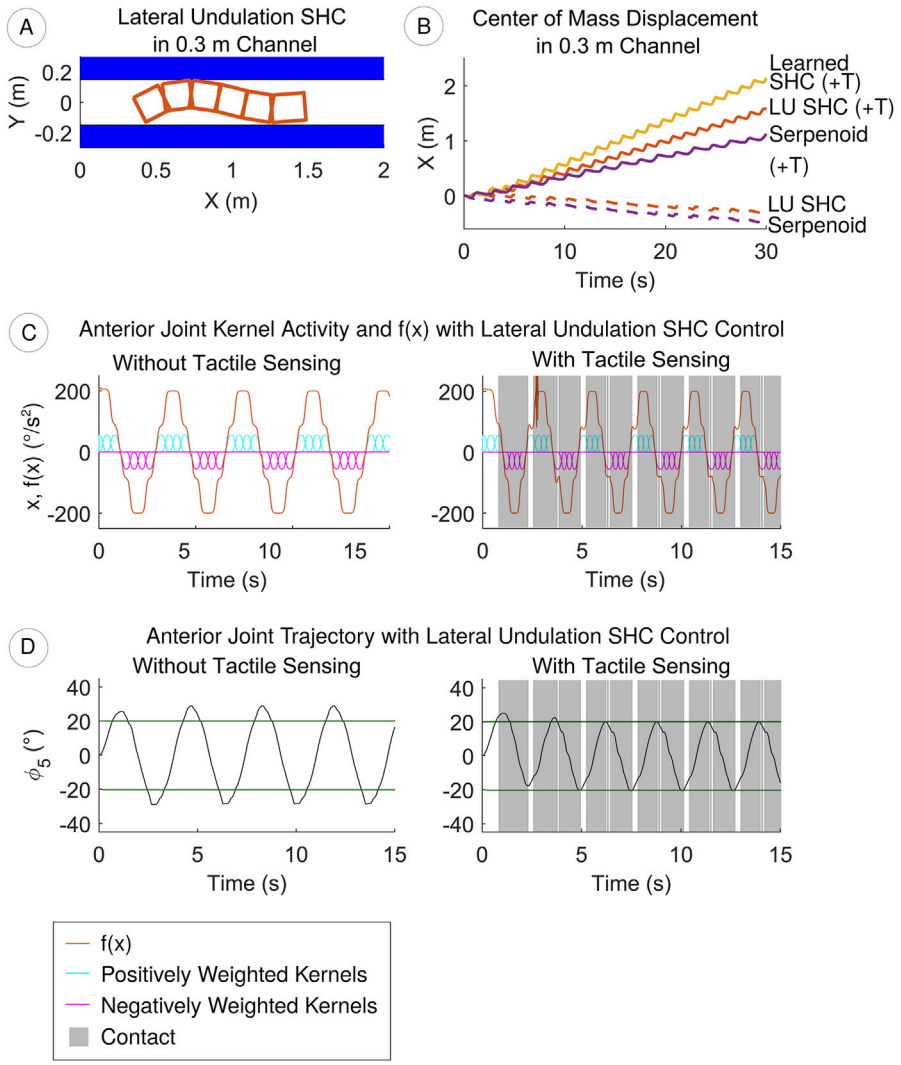

FIGURE 8
(A) Using lateral undulation SHC control with tactile sensing (+T), the robot moves through a 0.3 m channel **(B)** Tactile sensing improves the swimming speed through the channel, especially with learned SHC control **(C)** Contact detection increases the frequency of SHC kernels and $f(x)$, as shown for the lateral undulation gait **(D)** Increasing kernel frequency corresponds to faster, lower amplitude joint trajectories.

wall, moving opposite of the intended direction. Speed benefits of gait optimization in an obstacle-free environment are retained in this structured environment.To validate how the sensor integration impacts SHC-generated gaits, we examine the kernel activity. Tactile sensing increases the frequency of kernel activation, forcing term $f(x)$, and joint trajectories (Figures 8C, D). While the forcing term $f(x)$ achieves the same magnitude, the joints have less time to accelerate and therefore achieve lower amplitudes. The coupled frequency and amplitude adaptation enables the SHC controllers with tactile sensing to locomote more quickly than sensor-free implementations or the serpenoid (+T) controller, which only adapts joint amplitude.

The relative performance of the controllers depends on the width of the crevice (Figure 9). In the narrowest channels all controllers yield backwards net locomotion, as the robot incidentally pushes backwards against the walls. As channel width increases, forward velocity generally increases before saturating when the channels are wide enough that wall contact becomes negligible. Controllers that incorporate tactile sensing achieve forward progress at lower channel widths and maintain higher average velocities than their unsensorized counterparts. Moreover, the SHC controllers with tactile sensing achieve higher average velocities than the serpenoid (+T) controller, suggesting that the frequency and amplitude modulation is more effective than amplitude reduction alone. Consistent with results for the unimpeded swimming study, the learned SHC (+T) controller yields the highest velocity of all controllers in most regimes.

The advantages of tactile sensing are similarly evident from COT trends for narrow crevices (Figure 9). For the same channels, COTs for controllers equipped with tactile sensors are consistently lower than for controllers without. The lateral undulation and learned SHC controllers (+T) achieve similar efficiency to the serpenoid controller (+T) in channels narrower than approximately $0.45m$, and better efficiency in wider channels. While the learned SHC controller (+T) offers better speed, the lateral undulation SHC (+T) offers modestly better efficiency in some conditions. Based on the

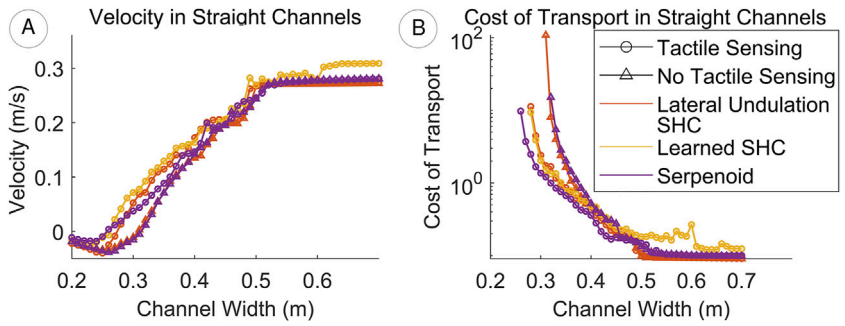

FIGURE 9
(A) Controllers yield backwards locomotion in the narrowest channels. Velocities increase until no wall contact occurs. The learned SHC controller (+T) permits faster swimming than both the lateral undulation SHC and serpenoid controllers **(B)** COT is defined only where the robot progresses forwards and decreases (i.e., locomotion becomes more efficient) as channel width increases. Tactile sensing reduces COT especially in narrow channels. While the learned gait generally improves speed, it sacrifices efficiency in some conditions.

improved average velocity and efficiency, we conclude that scaling kernel progression rates according to tactile data is an effective mechanism for improving SHC performance in straight, narrow channels.

3.3 Uneven channels

In uneven channels, contact detection remains crucial to the performance of the robot. Without tactile sensing, the serpenoid and SHC controllers cannot adapt the body shape and become trapped when the robot contacts both sides of the channel (Figure 10A). With tactile sensing, the controllers reduce the amplitude of the joints, narrowing the gait and allowing the robot to pass obstacles (see video in Supplementary Files). However, the robot may still not progress consistently if it comes into contact with an obstacle head on, for example, the lateral undulation SHC (+T) controller in Figure 10A. In this case, the robot continually retries forward motion, colliding with the channel wall until a more suitable approach configuration occurs by chance and the robot overcomes the obstacle. As in prior experiments, the learned SHC allows the greatest forward progress when it is not trapped in the channel (Figure 10).

In the complete set of channels, the serpenoid and SHC controllers with tactile sensing achieve greater progress than those without. Of 65 obstacles, our analyses include 59 (serpenoid), 65 (serpenoid (+T)), 62 (lateral undulation SHC), 64 (lateral undulation SHC (+T)), and 62 (learned SHC (+T)) data points. In 95% of cases where lateral undulation SHC controllers with and without sensing both produce valid results, the sensor equipped controller moves further through the channel. Similar results apply for the serpenoid controllers (98%). The coupled frequency and amplitude response in the lateral undulation (+T) and learned SHC (+T) controllers allow the robot to swim further compared with the serpenoid (+T) controller, as long as the robot does not become trapped in the channel (Figure 10). However, the SHC (+T) controllers also suffer from high variability in performance. The serpenoid controller (+T) shows continual progression in the most channels (62%), followed by the learned SHC (+T) and lateral undulation SHC (+T) (both 45%) controllers (Table 5). The learned SHC (+T) controller is more likely to recover from being trapped (e.g., intermittent progress, (27%) than the lateral undulation SHC (+T) controller (14%). Although the SHC controllers with tactile sensing are more likely to become trapped in uneven, confined spaces and operate less efficiently (see Figure 10D) than the serpenoid (+T) controller, they can achieve greater maximal forward progress.

Mean velocities are compared between controllers with a Kruskal–Wallis test, which indicates that one or more controllers differs ($p = 2.7 \times 10^{-30}$). Controller pairs are compared with Dunn test with a Šidák correction to account for multiple comparisons, using 95% confidence. The learned SHC (+T) controller outperforms the serpenoid controller (+T), achieving 28.8% higher velocity on average ($p = 0.014$) (See Figure 10C and Table 5). The learned SHC (+T) controller performs similarly to the lateral undulation SHC (+T) controller ($p = 0.31$), albeit with slightly higher average velocity and lower variance due to improved rate of recovery from entrapment. Overall, these results indicate that modulating SHC kernel activation rates based on tactile sensing is an effective approach for navigating uneven terrain, particularly when paired with gait optimization techniques.

Incorporating tactile sensing improves efficiency, as well as speed. A Kruskal–Wallis test shows significant differences between the controllers ($p = 6.8 \times 10^{-38}$), and we proceed with a Dunn-Šidák *post hoc* evaluation as before. Compared to the lateral undulation SHC controller without sensing, the learned SHC controller (+T) ($p = 9.0 \times 10^{-8}$) and lateral undulation SHC controller (+T) ($p = 2.3 \times 10^{-8}$) are more efficient. The learned and lateral undulation SHC controllers with sensing show similar efficiency ($p > 0.999$). However, the serpenoid controller (+T) is significantly more efficient than either the learned SHC (+T) ($p = 6.9 \times 10^{-4}$) or lateral undulation SHC controllers (+T) ($p = 1.8 \times 10^{-4}$) (Figure 10D). The elevated COT for the sensorized SHC controllers is likely because tactile input increases the joint oscillation frequency, which entails higher energy consumption. If the increased motion does not enable the robot to overcome an obstacle, efficiency declines. Reducing efficiency for increased velocity may be acceptable for robots that are powered via tether or have time sensitive objectives, as in search and rescue.

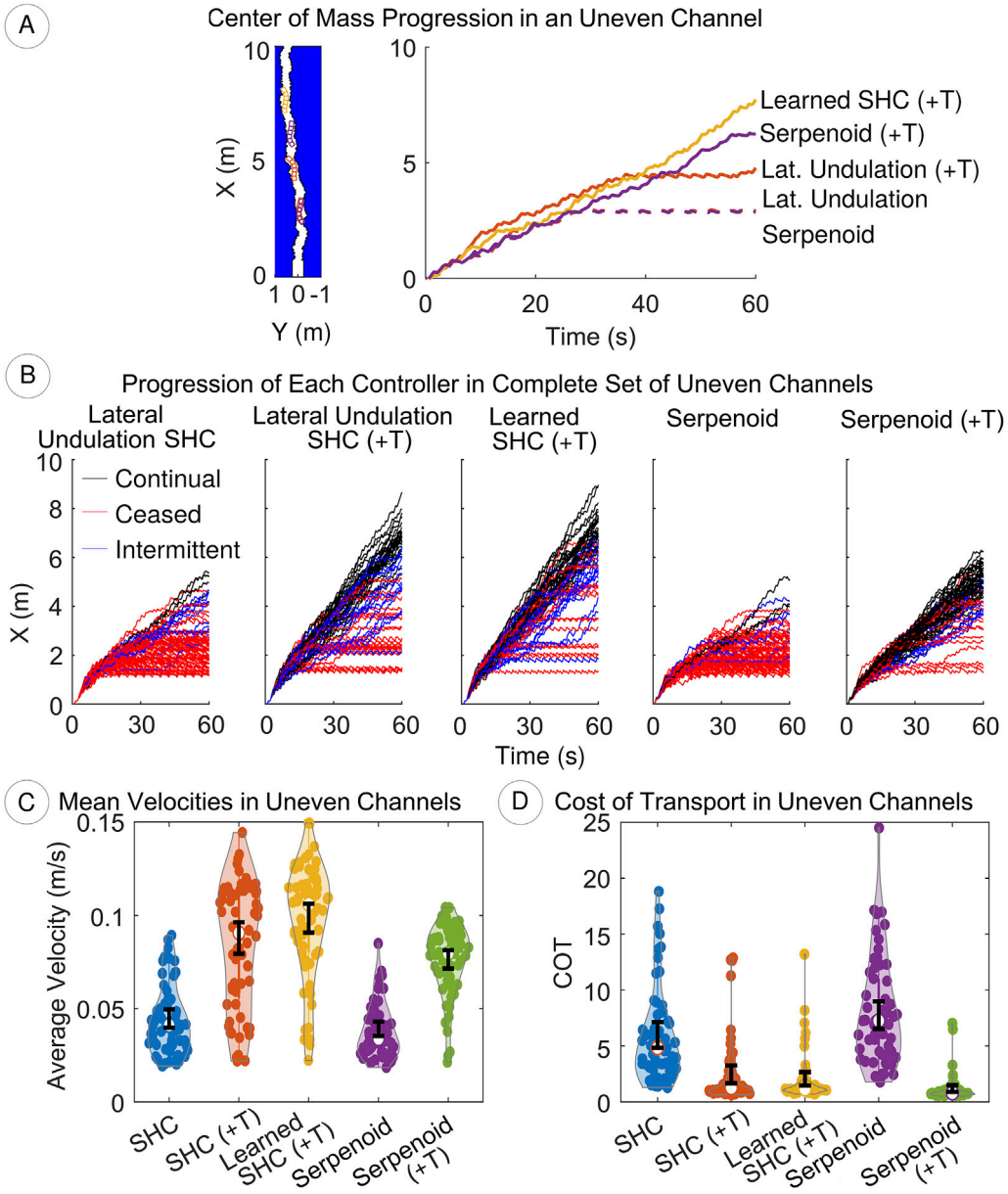

FIGURE 10
(A) Tactile sensing improves locomotion in uneven terrain, though many attempts may be needed if approach is sub-optimal (e.g., lateral undulation SHC (+T); see Supplementary Video) **(B)** We categorize progress for each trial as continual (black), ceased (red), or intermittent (blue). Lateral undulation SHC (+T) and learned SHC (+T) controllers progress faster, but are trapped more often than the serpenoid controller (+T) **(C, D)** Velocity and COT distributions (dots) are shown. 95% confidence intervals (black) are established with bias corrected and accelerated nonparametric bootstrapping ($n_{bootstrap} = 10,000$, convergence shown in Supplemental Materials). The learned SHC (+T) offers the greatest speed, though serpenoid control (+T) yields the lowest and most reliable COT. Violin plot code by Bechtold (2016).

4 Discussion

In this work, we implement movement primitives based on stable heteroclinic channels to control a simulated aquatic snake robot. The SHC controller provides comparable performance to a conventional serpenoid controller. We demonstrate that MP weights relate proportionally to joint trajectories by linearly scaling the weights from the lateral undulation SHC controller to achieve an anguilliform gait. We optimize the SHC controller by modeling the system dynamics and iteratively tuning the weights, resulting in a 12% speed increase when the robot swims in an obstacle-free environment. Furthermore, we show that modulating transitions between SHC kernels with tactile sensing adapts the gait frequency and amplitudes to improve locomotion in straight passages (Figure 8). Finally, we examine locomotion over a diverse set of randomly generated channels that are between 1.7 and 2.8 times wider than the robot, and wander laterally up to three times the robot width over the robot's length. Even for the most consistent controller examined (serpenoid (+T)), channel geometry considerably impacts velocity ($0.037\frac{m}{s} - 0.10\frac{m}{s}$) and cost of

TABLE 5 Uneven channel performance.

Controller	Progression categorization (%)			COT CI		Velocity CI	
	Continual	Intermittent	Ceased	Lower	Upper	Lower	Upper
Lateral Undulation SHC	6.6	15	79	4.86	7.17	0.040	0.050
Lateral Undulation SHC (+T)	45	20	34	1.68	3.24	0.079	0.096
Learned SHC (+T)	45	27	27	1.48	2.73	0.091	0.106
Serpenoid	5	10	85	6.54	9.05	0.036	0.043
Serpenoid (+T)	62	14	25	0.89	1.48	0.072	0.082

transport (0.56 − 2.4). Applying sensory information to regulate the pace of kernel transitions in SHC movement primitives improves average velocity by 25.3% compared to a serpenoid controller that only alters the gait amplitude during contact in a variety of uneven, confined environments. SHC movement primitives thus constitute a transparent, learnable, and adaptable framework for establishing rhythmic gaits.

Our research serves as a practical demonstration of controlling a nonlinear dynamical system with SHC movement primitives and adapting its behavior by incorporationg sensory information. By showing that the weight parameters in SHC movement primitive relate proportionally to the resulting joint trajectories, we provide a pathway for robot operators to intuitively visualize, alter, and design gaits. In optimized controllers, the same visualizations may permit operators to heuristically predict emergent behavior without extensive testing. Thus, the SHC movement primitive controller offers a transparent approach to modeling CPGs, enabling faster development of bio-inspired systems. The abstract, visualizable approach allows researchers to address how CPG modules, represented by saddle equilibria, interact with sensory inputs and other modules to produce complex rhythmic motor patterns.

The present work demonstrates that SHCs are a promising control framework for replicating rhythmic behavior, and suggests that other locomotion patterns may be constructed by tuning weights and modulating progression between kernels. Future research may examine more advanced methods for incorporating sensory feedback to adapt individual joint trajectories, rather than regulating the entire network. Investigating weights and arrangements of saddle equilibria that enable other gaits, such as concertina locomotion would also be worthwhile. Transitioning between gaits may be achievable by expanding upon research by Rouse and Daltorio (2024), which explores the effects of sensor noise on decision making. Additionally, integration of more complex sensory information, such as vision, for localization and long term path planning would be beneficial. The effects of multisensory joint adaptation and gait transitions could be analyzed in environments with abrupt directional changes or multiple paths, such as S or T-shaped channels. With these improvements, movement primitives based on SHCs may contribute to research in biology by providing a convenient method for abstractly modeling neurological functions that support locomotion without detailed simulation of underlying cellular dynamics.

Data availability statement

The raw data supporting the conclusions of this article will be made available by the authors, without undue reservation.

Author contributions

NM: Conceptualization, Formal Analysis, Funding acquisition, Investigation, Methodology, Visualization, Writing–original draft, Writing–review and editing. NR: Writing–review and editing. KD: Funding acquisition, Project administration, Resources, Supervision, Writing–review and editing.

Funding

The author(s) declare that financial support was received for the research, authorship, and/or publication of this article. This research would not be possible without funding from Department of Defense (DoD) through the National Defense Science & Engineering Graduate (NDSEG) Fellowship Program. Research was also supported by the National Science Foundation's CAREER award (2047330).

Acknowledgments

Additionally, we thank Dr. Hillel Chiel (Department of Biology, Case Western Reserve University) for reviewing and editing this work, as well as Dr. Zonghe Chua (Department of Electrical, Computer, and Systems Engineering, Case Western Reserve University) for advice on statistical analysis.

Conflict of interest

The authors declare that the research was conducted in the absence of any commercial or financial relationships that could be construed as a potential conflict of interest.

Generative AI statement

The author(s) declare that no Generative AI was used in the creation of this manuscript.

Publisher's note

Supplementary material

The Supplementary Material for this article can be found online at: https://www.frontiersin.org/articles/10.3389/felec.2025.1507644/full#supplementary-material

SUPPLEMENTARY VIDEO S1
A comparison of swimming behavior for SHC movement primitive and serpenoid controllers in an unobstructed environment.

SUPPLEMENTARY VIDEO S2
In a 0.3 m channel, tactile sensing improves performance for both SHC movement primitive and serpenoid controllers. SHC controllers undulate both at higher frequency and lower amplitude during contact, while the serpenoid controller only reduces amplitude.

SUPPLEMENTARY VIDEO S3
Tactile sensor input improves the robot's ability to navigate uneven terrain. However, the robot can still be stymied by obstacles. With sensing, the SHC controller tuned for lateral undulation becomes stuck (t~35 s), but ultimately recovers.

SUPPLEMENTARY FIGURE S1
When learning weight parameters via gradient descent for the SHC control system, the velocity and COT stabilize within about 150 iterations.

SUPPLEMENTARY FIGURE S2
Confidence intervals on cost of transport for experiments in uneven channels are constructed by bootstrapping. 10,000 iterations is sufficient to ensure convergence of both upper and lower bounds for any of the tested controllers.

SUPPLEMENTARY FIGURE S3
Bootstrapped confidence intervals for velocity in uneven channels converge within 10,000 iterations for all examined controllers.

References

Anastasiadis, A., Paez, L., Melo, K., Tytell, E. D., Ijspeert, A. J., and Mulleners, K. (2023). Identification of the trade-off between speed and efficiency in undulatory swimming using a bio-inspired robot. *Sci. Rep.* 13, 15032. doi:10.1038/s41598-023-41074-9

Andersson, O., Grillner, S., Lindquist, M., and Zomlefer, M. (1978). Peripheral control of the spinal pattern generators for locomotion in cat. *Brain Res.* 150, 625–630. doi:10.1016/0006-8993(78)90827-2

Ashwin, P., Karabacak, Ã., and Nowotny, T. (2011). Criteria for robustness of heteroclinic cycles in neural microcircuits. *J. Math. Neurosci.* 1, 13. doi:10.1186/2190-8567-1-13

Ashwin, P., and Postlethwaite, C. (2016). Quantifying noisy attractors: from heteroclinic to excitable networks. *SIAM J. Appl. Dyn. Syst.* 15, 1989–2016. doi:10.1137/16M1061813

Astley, H. C., and Jayne, B. C. (2007). Effects of perch diameter and incline on the kinematics, performance and modes of arboreal locomotion of corn snakes (Elaphe guttata). *J. Exp. Biol.* 210, 3862–3872. doi:10.1242/jeb.009050

Bechtold, B. (2016). Violin plots for matlab. doi:10.5281/zenodo.4559847

Bonardi, S., Moeckel, R., Sproewitz, A., Vespignani, M., and Ijspeert, A. J. (2012). "Locomotion through reconfiguration based on motor primitives for roombots self-reconfigurable modular robots," in *ROBOTIK 2012; 7th German conference on robotics*, 1–6.

Brecelj, T., and Petrič, T. (2023a). Stable heteroclinic channel networks for physical human-humanoid robot collaboration. *Sensors* 23, 1396. doi:10.3390/s23031396

Brecelj, T., and Petrič, T. (2023b). "Utilizing a phase state system for reliable physical assistance in human-humanoid robot collaboration," in *2023 21st international conference on advanced robotics (ICAR)*, 258–263. doi:10.1109/ICAR58858.2023.10406553

Chen, S., and Roth, A. (2023). Gait design of a novel arboreal concertina locomotion for snake-like robots. *ArXiv:2309.06000*. doi:10.48550/arXiv.2309.06000

Cheslet, J., Beaubois, R., Khoyratee, F., Kohno, T., Ikeuchi, Y., and Levi, T. (2024). "Biomimetic snake locomotion using Central Pattern Generators network and bio-hybrid robot perspective," in *Isarob* (Beppu, Japan).

Cropper, E. C., Evans, C. G., Hurwitz, I., Jing, J., Proekt, A., Romero, A., et al. (2004). Feeding neural networks in the mollusc Aplysia. *Neurosignals* 13, 70–86. doi:10.1159/000076159

Daltorio, K. A., Boxerbaum, A. S., Horchler, A. D., Shaw, K. M., Chiel, H. J., and Quinn, R. D. (2013). Efficient worm-like locomotion: slip and control of soft-bodied peristaltic robots. *Bioinspiration and Biomimetics* 8, 035003. doi:10.1088/1748-3182/8/3/035003

[Dataset] Rouse, N., Horchler, A., Chiel, H., and Daltorio, K. (2024). *Sttable heteroclinic channels as a decision-making model: overcoming low signal-to-noise ratio with mutual inhibition*.

Dehghani, M., and Mahjoob, M. J. (2009). "A modified serpenoid equation for snake robots," in *2008 IEEE international conference on robotics and biomimetics*, 1647–1652. doi:10.1109/ROBIO.2009.4913248

Fod, A., Matarić, M. J., and Jenkins, O. C. (2002). Automated derivation of primitives for movement classification. *Aut. Robots* 12, 39–54. doi:10.1023/A:1013254724861

Giszter, S. (2015). Motor primitives—new data and future questions. *Curr. Opin. Neurobiol.* 33, 156–165. doi:10.1016/j.conb.2015.04.004

Gray, J. (1946). The mechanism of locomotion in snakes. *J. Exp. Biol.* 23, 101–120. doi:10.1242/jeb.23.2.101

Grillner, S., and Wallén, P. (2010). "The lamprey locomotor central pattern generator," in *Handbook of brain microcircuits*. Editors D. Shepherd, S. Grillner, and P. Gordon (Oxford University Press). doi:10.1093/med/9780195389883.003.0032

Guertin, P. A. (2013). Central pattern generator for locomotion: anatomical, physiological, and pathophysiological considerations. *Front. Neurology* 3, 183. doi:10.3389/fneur.2012.00183

Harris-Warrick, R. M. (2010). General principles of rhythmogenesis in central pattern generator networks. *Prog. Brain Res.* 187, 213–222. doi:10.1016/B978-0-444-53613-6.00014-9

Hoffmann, H., Pastor, P., Park, D.-H., and Schaal, S. (2009). "Biologically-inspired dynamical systems for movement generation: automatic real-time goal adaptation and obstacle avoidance," in *2009 IEEE international conference on robotics and automation*, 2587–2592. doi:10.1109/ROBOT.2009.5152423

Horchler, A. D., Daltorio, K. A., Chiel, H. J., and Quinn, R. D. (2015). Designing responsive pattern generators: stable heteroclinic channel cycles for modeling and control. *Bioinspiration and Biomimetics* 10, 026001. doi:10.1088/1748-3190/10/2/026001

Huang, Z., Kong, D., Ren, C., Li, S., and Ma, S. (2019). "Performance study of an underwater snake-like robot with a flexible caudal fin," in *2019 IEEE international conference on mechatronics and automation (ICMA)*, 1–5. doi:10.1109/ICMA.2019.8816412

Hunt, A., Szczecinski, N., and Quinn, R. (2017). Development and training of a neural controller for hind leg walking in a dog robot. *Front. Neurorobotics* 11, 18. doi:10.3389/fnbot.2017.00018

Ijspeert, A. J. (2008). Central pattern generators for locomotion control in animals and robots: a review. *Neural Netw.* 21, 642–653. doi:10.1016/j.neunet.2008.03.014

Ijspeert, A. J., Crespi, A., Ryczko, D., and Cabelguen, J.-M. (2007). From swimming to walking with a salamander robot driven by a spinal cord model. *Science* 315, 1416–1420. doi:10.1126/science.1138353

Ijspeert, A. J., Nakanishi, J., Hoffmann, H., Pastor, P., and Schaal, S. (2013). Dynamical movement primitives: learning attractor models for motor behaviors. *Neural Comput.* 25, 328–373. doi:10.1162/NECO_a_00393

Jayne, B. C. (2020). What defines different modes of snake locomotion? *Integr. Comp. Biol.* 60, 156–170. doi:10.1093/icb/icaa017

Kelasidi, E., Jesmani, M., Pettersen, K. Y., and Gravdahl, J. T. (2018). Locomotion efficiency optimization of biologically inspired snake robots. *Appl. Sci.* 8, 80. doi:10.3390/app8010080

Kelasidi, E., Pettersen, K. Y., Gravdahl, J. T., and Liljebäck, P. (2014). "Modeling of underwater snake robots," in *2014 IEEE international conference on robotics and automation (ICRA)*, 4540–4547. doi:10.1109/ICRA.2014.6907522

Kelasidi, E., Pettersen, K. Y., Gravdahl, J. T., Strømsøyen, S., and Sørensen, A. (2017). "Modeling and propulsion methods of underwater snake robots," in *2017 IEEE conference on control technology and applications (CCTA)*, 819–826. doi:10.1109/CCTA.2017.8062561

Kober, J., and Peters, J. (2009). "Learning motor primitives for robotics," in *2009 IEEE international conference on robotics and automation*, 2112–2118. doi:10.1109/ROBOT.2009.5152577

Kong, L.-H., He, W., Chen, W.-S., Zhang, H., and Wang, Y.-N. (2023). Dynamic movement primitives based robot skills learning. *Mach. Intell. Res.* 20, 396–407. doi:10.1007/s11633-022-1346-z

Lissmann, H. W. (1950). Rectilinear locomotion in a snake (Boa occidentalis). *J. Exp. Biol.* 26, 368–379. doi:10.1242/jeb.26.4.368

Marder, E., and Eisen, J. S. (1984). Electrically coupled pacemaker neurons respond differently to same physiological inputs and neurotransmitters. *J. Neurophysiology* 51, 1362–1374. doi:10.1152/jn.1984.51.6.1362

Marques, F., Flores, P., Claro, J., and Lankarani, H. (2016). A survey and comparison of several friction force models for dynamic analysis of multibody mechanical systems. *Nonlinear Dyn.* 86, 1407–1443. doi:10.1007/s11071-016-2999-3

McCormack, A., and Godfrey, K. (1998). Rule-based autotuning based on frequency domain identification. *IEEE Trans. Control Syst. Technol.* 6, 43–61. doi:10.1109/87.654876

Moreno, R., and Gomez, J. (2011). "Central pattern generators and hormone inspired messages: a hybrid control strategy to implement motor primitives on chain type modular reconfigurable robots," in *2011 IEEE international conference on robotics and automation*, 1014–1019. doi:10.1109/ICRA.2011.5980149

Mosauer, W. (1932). On the locomotion of snakes. *Science* 76, 583–585. doi:10.1126/science.76.1982.583

Norman-Tenazas, R. (2021). *Robust snake robot control via A spiking neuron central pattern generator*. Baltimore, MD: Johns Hopkins University. Master's thesis.

Ostrowski, J., and Burdick, J. (1996). Gait kinematics for a serpentine robot. In , *Proceedings of IEEE international conference on robotics and automation*. 1294–1299. doi:10.1109/ROBOT.1996.506885

Paraschos, A., Daniel, C., Peters, J. R., and Neumann, G. (2013). "Probabilistic movement primitives," in *Advances in neural information processing systems* (San Diego, CA: Neural Information Processing Systems, Inc.), 26.

Pastor, P., Hoffmann, H., Asfour, T., and Schaal, S. (2009). "Learning and generalization of motor skills by learning from demonstration," in *2009 IEEE international conference on robotics and automation*, 763–768. doi:10.1109/ROBOT.2009.5152385

Piñeirua, M., Godoy-Diana, R., and Thiria, B. (2015). Resistive thrust production can be as crucial as added mass mechanisms for inertial undulatory swimmers. *Phys. Rev. E* 92, 021001. doi:10.1103/PhysRevE.92.021001

Rabinovich, M. I., Huerta, R., Varona, P., and Afraimovich, V. S. (2006). Generation and reshaping of sequences in neural systems. *Biol. Cybern.* 95, 519–536. doi:10.1007/s00422-006-0121-5

Riddle, S., Jackson, C., Daltorio, K. A., and Quinn, R. D. (2023). "A dynamic simulation ofÂ aÂ compliant worm robot amenable toÂ neural control," in *Biomimetic and biohybrid systems*. Editors F. Meder, A. Hunt, L. Margheri, A. Mura, and B. Mazzolai (Cham: Springer Nature Switzerland), 338–352. doi:10.1007/978-3-031-38857-6_25

Rollinson, D., and Choset, H. (2013). "Gait-based compliant control for snake robots," in *2013 IEEE international conference on robotics and automation*, 5138–5143. doi:10.1109/ICRA.2013.6631311

Rouse, N., and Daltorio, K. (2024). Stable heteroclinic channel-based movement primitives: tuning trajectories using saddle parameters. *Appl. Sci.* 14, 2523. doi:10.3390/app14062523

Rouse, N. A., and Daltorio, K. A. (2021). Visualization of stable heteroclinic channel-based movement primitives. *IEEE Robotics Automation Lett.* 6, 2343–2348. doi:10.1109/LRA.2021.3061382

Sato, M., Fukaya, M., and Iwasaki, T. (2002). Serpentine locomotion with robotic snakes. *IEEE Control Syst. Mag.* 22, 64–81. doi:10.1109/37.980248

Schaal, S. (2006). "Dynamic movement primitives -A framework for motor control in humans and humanoid robotics," in *Adaptive motion of animals and machines*. Editors H. Kimura, K. Tsuchiya, A. Ishiguro, and H. Witte (Tokyo: Springer), 261–280. doi:10.1007/4-431-31381-8_23

Shaw, K. M., Lyttle, D. N., Gill, J. P., Cullins, M. J., McManus, J. M., Lu, H., et al. (2015). The significance of dynamical architecture for adaptive responses to mechanical loads during rhythmic behavior. *J. Comput. Neurosci.* 38, 25–51. doi:10.1007/s10827-014-0519-3

Sherrington, C. S. (1910). Flexion-reflex of the limb, crossed extension-reflex, and reflex stepping and standing. *J. Physiology* 40, 28–121. doi:10.1113/jphysiol.1910.sp001362

Shigeo, H. (1994). Biologically inspired robots: snake-like locomotors and manipulators by Shigeo hirose oxford university press, oxford, 1993, 220*pages, incl. Index* (£40). *Robotica* 12, 282. doi:10.1017/S0263574700017264

Simoni, M. F., and DeWeerth, S. P. (2007). Sensory feedback in a half-center oscillator model. *IEEE Trans. Biomed. Eng.* 54, 193–204. doi:10.1109/TBME.2006.886868

Tagliabue, M., Ciancio, A. L., Brochier, T., Eskiizmirliler, S., and Maier, M. A. (2015). Differences between kinematic synergies and muscle synergies during two-digit grasping. *Front. Hum. Neurosci.* 9, 165. doi:10.3389/fnhum.2015.00165

Tesch, M., Lipkin, K., Brown, I., Hatton, R., Peck, A., Rembisz, J., et al. (2009). Parameterized and scripted gaits for modular snake robots. *Adv. Robot.* 23, 1131–1158. doi:10.1163/156855309X452566

Thandiackal, R., Melo, K., Paez, L., Herault, J., Kano, T., Akiyama, K., et al. (2021). Emergence of robust self-organized undulatory swimming based on local hydrodynamic force sensing. *Sci. Robotics* 6, eabf6354. doi:10.1126/scirobotics.abf6354

Travers, M., Gong, C., and Choset, H. (2015). "Shape-constrained whole-body adaptivity," in *2015 IEEE international symposium on safety, security, and rescue robotics (SSRR)*, 1–6. doi:10.1109/SSRR.2015.7442945

Travers, M., Whitman, J., and Choset, H. (2018). Shape-based coordination in locomotion control. *Int. J. Robotics Res.* 37, 1253–1268. doi:10.1177/0278364918761569

Tresch, M. C., and Bizzi, E. (1999). Responses to spinal microstimulation in the chronically spinalized rat and their relationship to spinal systems activated by low threshold cutaneous stimulation. *Exp. Brain Res.* 129, 0401–0416. doi:10.1007/s002210050908

Wang, J., Ouyang, W., Gao, W., and Ren, Q. (2017a). "Locomotion control of a serpentine crawling robot inspired by central pattern generators," in *2017 asia-pacific signal and information processing association annual summit and conference (APSIPA ASC)*, 414–419. doi:10.1109/APSIPA.2017.8282067

Wang, Z., Gao, Q., and Zhao, H. (2017b). CPG-inspired locomotion control for a snake robot basing on nonlinear oscillators. *J. Intelligent and Robotic Syst.* 85, 209–227. doi:10.1007/s10846-016-0373-9

Yu, J., Tan, M., Chen, J., and Zhang, J. (2014). A survey on CPG-inspired control models and system implementation. *IEEE Trans. Neural Netw. Learn. Syst.* 25, 441–456. doi:10.1109/TNNLS.2013.2280596